Microfluidic Surface Shields: Control of Flow and Diffusion over Sensitive Surfaces

Oscar Boyadjian,[1] Etienne Boulais,[2] and Thomas Gervais[1,2,*]

[1] *Biomedical Engineering Institute, Polytechnique Montreal, Montreal, Quebec, H3T 1J4 Canada*
[2] *Engineering Physics Department, Polytechnique Montreal, Montreal, Quebec, H3T 1J4 Canada*

(Received 21 November 2020; revised 11 October 2021; accepted 30 November 2021; published 11 January 2022)

Selective shielding of surfaces from flow and diffusion is essential in many domains of physics and engineering. We propose and characterize experimentally a framework to shield both flow and diffusion simultaneously within a reshapable fluid volume. To do so, we directly use flow singularities to generate conformal transforms of the diffusion profile, taking inspiration from classical cloaking devices. The properties of microfluidic surface shields as open-space diffusion filters (*O*-filters) are further investigated. An analytical model is provided, which yields an outstanding match with experimental measurements of both flow and tracer diffusion. Via conformal mapping, these measurements reveal a strong topological link with classical *H*-filters in microfluidics.

DOI: 10.1103/PhysRevApplied.17.014012

I. INTRODUCTION

Precise control of fluid-surface interactions is crucial for many applications in the domains of chemical synthesis and catalysis [1,2], biosurfaces [3], chip cooling [4], and sensors [5]. Namely, they depend on accurately conveying a fluid flow and its transport of heat, momentum, shear, or chemical species to a sensitive or reactive surface. In such experiments, there is a need for selective exposure (or protection) of a segment of a surface to an incoming flow. Ideally, exposure of the surface will be flexible and adjustable in real time, so that the surface can be sequentially shielded and exposed.

The conceptual problem of isolating a finite region from an incoming flux has been explored thoroughly in the domain of metamaterials and cloaking. Initially introduced by Leonhardt [6] and Pendry *et al.* [7], optical cloaking broadly consists of the engineering of metamaterials to effect a conformal transform of incoming electromagnetic waves and direct them around a shielded obstacle. The general idea, termed cloaking, was quickly transposed to other wavelike phenomena, starting with acoustic waves [8,9], but eventually being applied to elastic waves [10,11], seismic waves [12], fluid surface waves [13], and even quantum-mechanical matter waves [14], as well as a number of physics not bound by parabolic wave equations but still underpinned by conformally invariant equations, such as heat diffusion in solid bodies [15,16], chemical cloaking [17], or flow in porous media [18]. In cloaking applications, the conformal transform is generally hardwired into the substrate of the material, making real-time transformation of the incoming field difficult.

In many applications involving fluid processors, the goal is not to cloak an object from a flow field, but rather to prevent a fluid phase, containing a certain scalar species (typically reagents or temperature), from interacting with part of a surface by dynamically deflecting it with minimal perturbation of the flow profile downstream. To achieve this, we take inspiration from the vast literature on cloaking phenomena and keep the idea of generating a conformal transform on an incoming flow to reroute it around an obstacle, thus selectively shielding it from incoming heat or reactive species. For such a strategy to function, the underlying equations describing our device have to be invariant under conformal transforms. This is the case for steady-flow diffusion in Hele-Shaw cells, that is, low-Reynolds flow confined to a quasiplanar region between two plates. The close analogy between streamlines in Hele-Shaw cells and electric field lines in two-dimensional (2D) space [19] also hint at the use of tunable-flow singularities to directly generate a conformal mapping of flow and concentration around the obstacle.

Here, we give a proof of concept that a reshapable excluded region can be generated in a microfluidic chamber. Rather than using an etched substrate to generate the conformal map, like classical cloaking setups would, we follow recent work of our group in the domain of multipolar microfluidics [20,21] and directly use flow singularities to deform the incoming fluid flow. When the flow singularities have net-zero inflow, the excluded zone forms a

*thomas.gervais@polymtl.ca

Rankine body, which is known to induce a net-zero drag, thus no detectable measurable pressure drop downstream, a property reminiscent of cloaking mechanisms. Since the setup includes finite-diffusion effects, there remains a thin boundary layer, which allows exchange between the shielded region and the incoming flow. We show how, at high Peclet numbers, this boundary layer can be made arbitrarily thin, and shielding can be made "perfect," if the reactive surface does not overlap with it. Alternatively, if filtering is desired, we show how this boundary layer can be modulated in real time to enable controlled exchange between the two regions without inducing any hydrodynamic perturbation in the far field. In this regime, the device functions like an open-space analog to the well-known microfluidic H-filter [22]. We also show how the system can be used to send controlled pulses of chemical reagents downstream, allowing for the generation of precise "trains" of chemical concentration.

II. THEORY AND EXPERIMENTAL RESULTS

In classical fluid mechanics, the interaction of a plane flow with two or more mass-balanced injecting and aspirating point sources generates an exclusion zone in a flow stream called a Rankine body. They have been studied extensively to minimize the drag in ship hulls [23] or to model groundwater heat pumps [24,25]. They can be created using tailored surface-charge patterns in electro-osmotic flows [26]. The simplest Rankine bodies are obtained by aligning a pair of mass-balanced injection and aspiration apertures, or doublet, in line with an incident stream [Figs. 1(a) and 1(b)]. We fabricate a microfluidic device able to generate Rankine bodies using four tubes connected to syringe pumps; a glass slide; and a 3D-printed central cell that is $W = 1.6$ cm wide, $L = 2$ cm long, and $G = 500$ μm deep, pierced in its center by two circular apertures of $a = 135$ μm in diameter that are $d = 1$ mm apart from each other [Fig. 1(c)]. The various parts of this device are sealed together with UV-sensitive glue, and dilute fluorescent beads (3 μm in diameter) and dyes [fluorescein isothiocyanate (FITC) and tetramethylrhodamine (TRITC)] in a water-ethanol mixture are injected in the device to enable flow and transport visualization, respectively [Figs. 1(b) and 1(d)]. The device thus forms a Hele-Shaw cell of depth $G \ll (W, L)$ in which a central recirculation zone circling the apertures forms within the lateral flow, from which diffusive tracers can escape or enter by diffusion [Fig. 1(d)].

The effects of the lateral walls on velocity are negligible in our experiments (see Appendix A), so the complex flow potential for our two-aperture configuration can be expressed classically in terms of a single complex variable, $z = x + iy$, by superposing two-point sources and an incident stream in a Hele-Shaw cell:

$$\Phi(z) = \frac{Q_{\text{inc}}}{WG} z + \frac{Q_{\text{inj}}}{2\pi G}\left[\ln\left(z + \frac{d}{2}\right) - \ln\left(z - \frac{d}{2}\right)\right], \tag{1}$$

where Q_{inc} and Q_{inj} are the flow rates of the incident stream and at the apertures, respectively, and are on the order of 1 μL/s. The chamber's Reynolds number is about 0.001, which ensures a viscous-driven (Stokes) flow regime. Making Eq. (1) dimensionless yields

$$\tilde{\Phi}(\tilde{z}) = \beta\tilde{z} + \ln(\tilde{z} + 1) - \ln(\tilde{z} - 1), \tag{2}$$

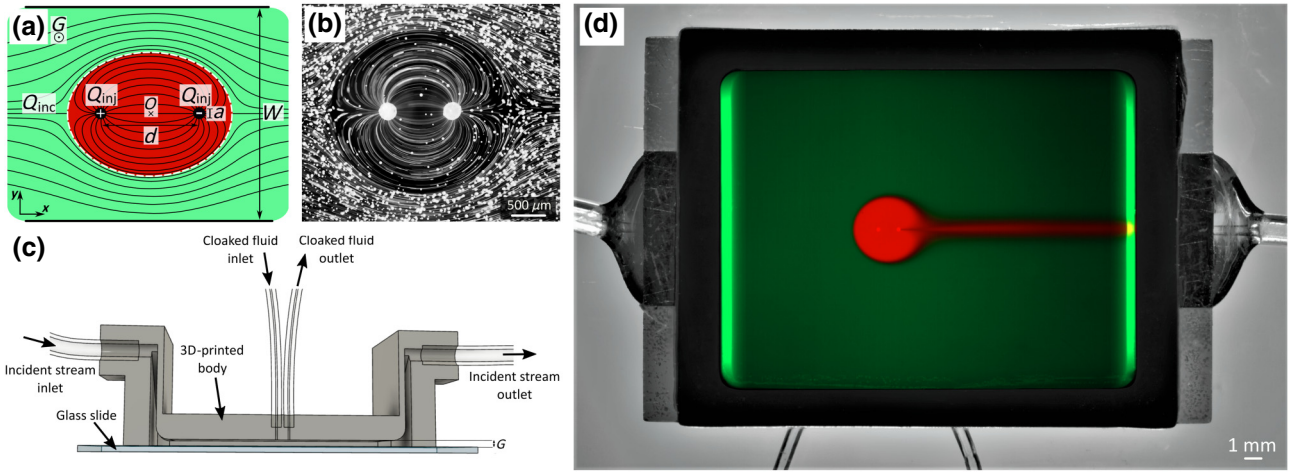

FIG. 1. Microfluidic surface-shield paradigm. (a) Annotated schematic representation of flow in the device. (b) Experimental picture of streamlines. (c) Cutaway computer-aided design drawing of the experimental device. (d) Picture of an operating surface shield visualized by injecting fluorescein in the incident stream (green) and Rhodamine B in the recirculation zone (red). Black strips may be due to Förster resonance energy transfer (FRET) occurring between these two fluorophores [27].

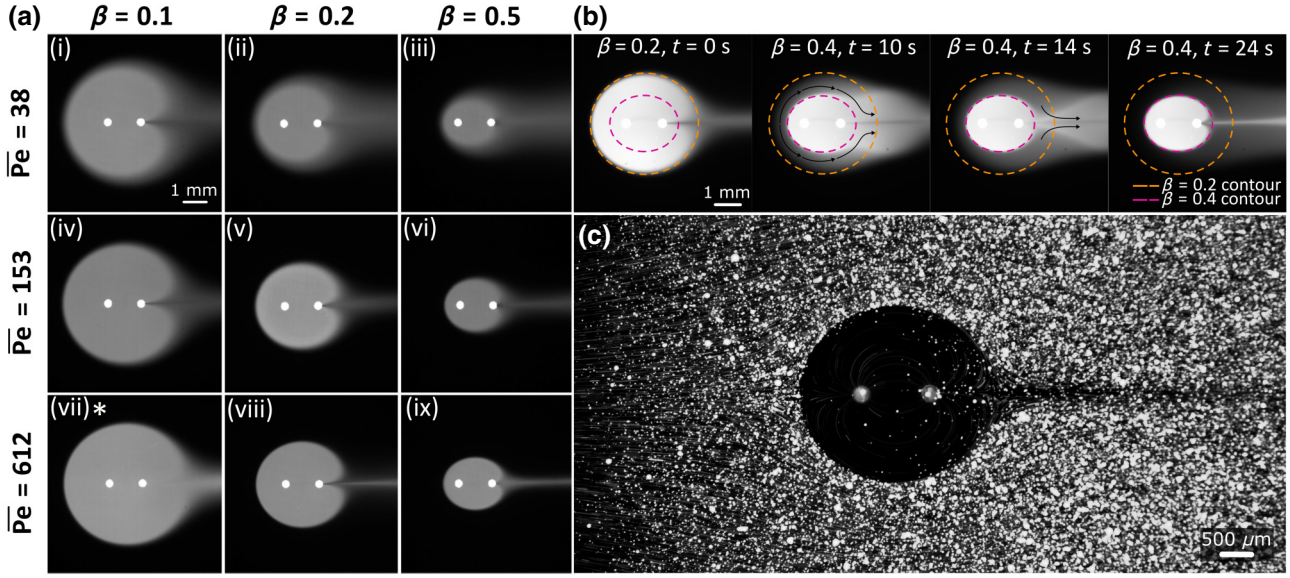

FIG. 2. Control of the shielded region. (a) (i)–(ix) Mosaic of experimental results displaying the various shielded shapes, depending on β and $\overline{\mathrm{Pe}}$. * This configuration is distorted by a lack of luer-lock airtightness during the experiment, yielding an actual $\overline{\mathrm{Pe}}$ of 367. (b) Experimental response when β is a step function suddenly varying from 0.2 to 0.4. (c) Experimental picture of an area protected from a fluorescent-bead stream for 38 min. Wide luminous dots show adsorbed bead bundles.

in which the dimensionless velocity ratio, $\beta = \pi d Q_{\mathrm{inc}}/WQ_{\mathrm{inj}}$, appears and dictates the size of the Rankine body. To simplify the notation from here on, we use Φ to refer to the dimensionless potential [Eq. (2)]. In such a configuration, a closed ellipsoidal recirculation zone isolated from the rest of the stream appears. In the particular case of an infinite 2D medium, the interface between two fluids undergoes a slip-boundary condition, and the obstacle generates no drag, as per d'Alembert's paradox [28]. Simple scaling laws further reveal that, when the medium is bound by lateral walls, the drag rises only as the square of the blockage ratio. Such second-order correction is negligible in typical experimental situations (see Appendix B). This recirculation zone is thus a 2D cloaking analog, as velocity and pressures as flow variables are not disturbed by it from afar. One key difference remains, however, in that velocity and pressure invariance is not omnidirectional, as it is the case in cloaking. It exists only when the flow is aligned parallel to the flow apertures.

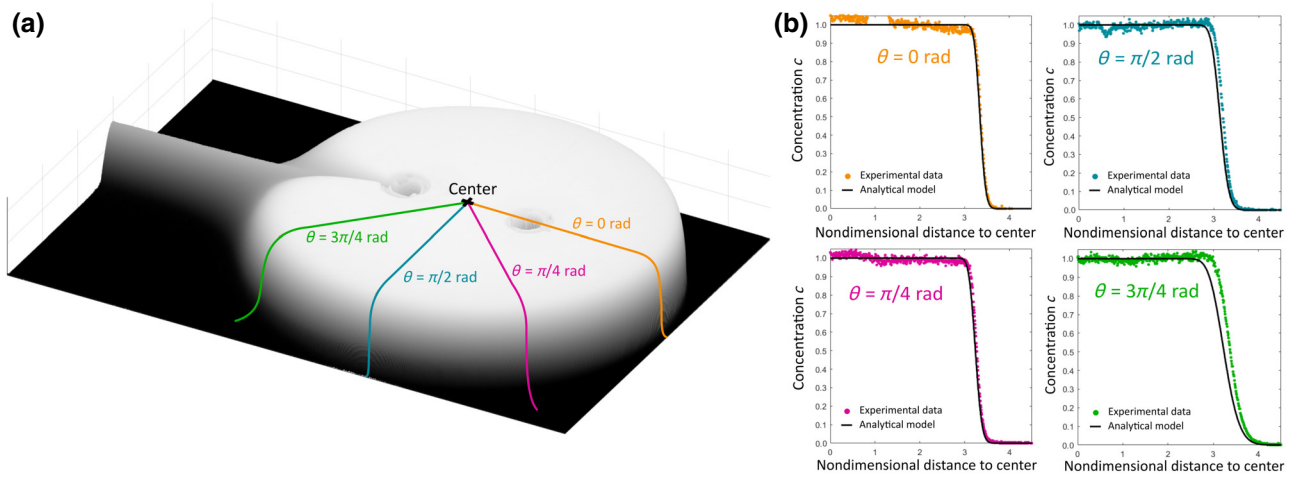

FIG. 3. Convection-diffusion within the device. (a) Visualizing an experimental concentration map as a surface plot (height is proportional to concentration). (b) Comparison between experimental concentration map and the model obtained with Eq. (4) at various angles.

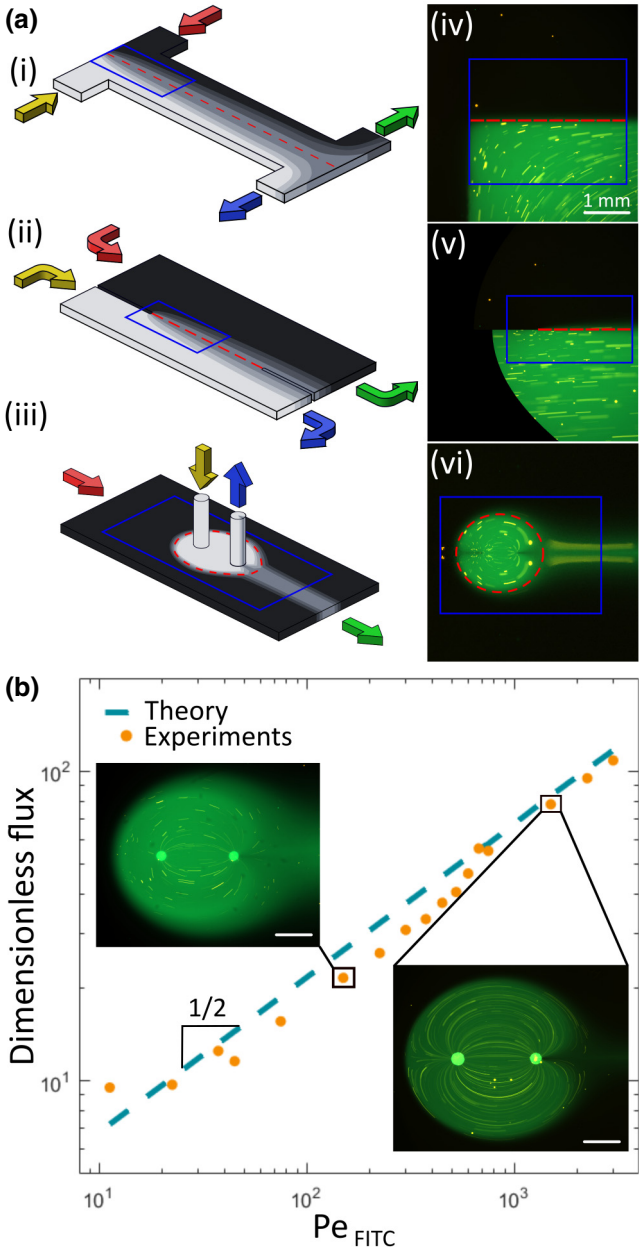

FIG. 4. Conformal analogy between the microfluidic surface shield and the H-filter. (a) Drawings of (i) H-filter domains, (ii) streamline-coordinate domain, and (iii) Rankine-flow domain. Associated experimental domains: (iv) experimental picture of transport within an H-filter, (v) same picture transformed first to streamline coordinates and then (vi) to the Rankine domain. b) Power law between dimensionless flux and Peclet number. Insets, at low Pe, the shield can filter FITC from beads by allowing the former to diffuse downstream (top left) and, at higher Pe, isolate both species from the surroundings (bottom right). Scale bars correspond to 1 mm. It should be noted that $\mathrm{Pe}_{\mathrm{beads}} \sim 4 \times 10^3\ \mathrm{Pe}_{\mathrm{FITC}}$.

The concentration profile in this microfluidic device is, in turn, determined by the 2D steady-state convection-diffusion equation:

$$\Delta c + \mathrm{Pe}\nabla\Phi \cdot \nabla c = 0, \tag{3}$$

where $\mathrm{Pe} = Q_{\mathrm{inj}}/2\pi GD$ is the Peclet number (D denotes either thermal or mass diffusivity), which is usually high (above 100) in microfluidics. As it turns out, Eq. (3) in the context of 2D Hele-Shaw microfluidics is one of the handful of equations beyond Laplace's equation that are naturally conformally invariant [29]. By using a transformation to streamline coordinates, $(\varphi, \psi) = [Re(\Phi), \mathrm{Im}(\Phi)]$, the problem becomes that of two incoming plane flows separated by a horizontal obstacle (see Appendix C).

At high Peclet numbers, the problem becomes similar to the problem of convection-diffusion around a finite absorber, for which no simple analytical solution exists [30]. We can, however, obtain a concise closed-form solution for high-Peclet-number flows that is valid near the leading edge of the shielded region.

The solution [29,31] is given by

$$c(\varphi,\psi) = \begin{cases} \frac{1}{2}\left\{1 - \mathrm{erf}\left[\mathrm{Im}\left(\sqrt{\mathrm{Pe}\Phi}\right)\right]\right\}, & \psi < 0, \\ \frac{1}{2}\left\{1 + \mathrm{erf}\left[\mathrm{Im}\left(\sqrt{\mathrm{Pe}\Phi}\right)\right]\right\}, & \psi \geq 0. \end{cases} \tag{4}$$

We see at once that, provided the chamber is large enough, only two parameters are needed to fully describe the profile of the shielded region: the velocity ratio, β, to account for fluid-flow effects, and the Peclet number for diffusion. They can be varied independently to entirely decouple the protected region's shape and the amount of diffusive loss. The shielded volume and interfacial diffusion can be modified very easily by varying both β and Pe, as shown in Fig. 2(a)(i)–(ix). Following Ref. [32], the images are sorted according to the local Peclet number:

$$\overline{\mathrm{Pe}} = \mathrm{Pe}\beta^2\sqrt{1 + 2/\beta}, \tag{5}$$

which ensures a comparable diffusion length for images of similar $\overline{\mathrm{Pe}}$. From Eq. (1), the surface shield's horizontal "major axis" and vertical "minor axis" can also be extracted and show good agreement with experimental values (see Appendix D).

As shown in Figs. 1(d) and 2(a), the transport aspect of surface shielding is always limited by a diffusion-boundary layer around the Rankine body. This "imperfection" can be made arbitrarily small by increasing the Peclet number while maintaining β constant [Fig. 2(a)]. This is reminiscent of a similar property in optical cloaks, where the obstacle is never rendered totally invisible but rather made arbitrarily thin, in such a way that its surface is imperceptible by geometrical optics [1]. "Perfect" shielding can also be achieved by ensuring that the shielded surface does not overlap with the diffusion-boundary layer (see Appendix E). Also, when the interaperture distance is short enough, there is a perfect correspondence between the streamlines of our microfluidic system and the light path in optical cloaks [1]. In this sense, the flow- and transport-shielding framework introduced here constitutes

the basis of what we may call "transformation microfluidics," by analogy with transformation thermodynamics [15] or transformation optics [1,7].

III. TRANSIENT ASPECTS

Practically, the main interest in generating devices that can isolate zones from incoming flow lies in the ability to modify the exposure of a surface to outer flow, such that parts of a sensitive area can be exposed at times and protected from it at others. This drives us to consider the transient aspects of transport in the device. To do so, we experimentally study the transition within the shield from one steady state to another following an abrupt change in the dimensionless velocity ratio, β (Appendix F). We observe that the transient time governing the variation in the shielded area is described by the simple convective timescale, $t_c \sim L/U = 15$ s, where L is the shielded region's semimajor axis and U is the characteristic velocity. Meanwhile, the diffusive characteristic time is here on the order of $t_d \sim L^2/D = 1.6$ h. The large difference between these timescales ensures efficient shielding at high Peclet numbers, as chemical exchange between the shield and its surroundings is prevented. Alternatively, we can deliver downstream reagent pulses by varying β [Fig. 2(b)]. Overall, the stability of the steady states over time without significant fluctuations between transitions is also demonstrated, allowing us to protect a surface from undesired adsorption [Fig. 2(c)].

IV. DISCUSSION

The concentration profiles obtained from Eq. (4) yield outstanding agreement with experimental measurements up to very close to the device's diffusive tail at moderate-to-high Pe [Figs. 3(a) and 3(b)]. Since Eq. (4) is a solution of conformally invariant Eq. (3), it follows that this match will be maintained under similar conditions in any other device geometry obtained via a conformal transform of the current one [21]. In this manner, by transforming the double-shielding geometry to streamline coordinates, and then using Schwarz-Christoffel mapping, we find that the microfluidic shielding mechanism is a conformal analog of the H-filter [Fig. 4(a)], one of the most recognized devices in the field of microfluidics [33]. The close analogy between the H-filter and the microfluidic surface shield suggests the latter can also be used as a type of diffusion-based open-space filter or "O-filter," as evidenced by the experimental extraction of FITC molecules from a FITC–fluorescent-bead mixture [Fig 4(b), insets]. Inspection of the dimensionless diffusive flux (or Sherwood number) around the Rankine body further reveals that it scales as $\sqrt{\text{Pe}}$ [Fig. 4(b)], as would be expected for conformally analog filtration processes arising both from transport at a slip-flow interface, such as in H-filters [34]. Contrary to H-filters, O-filters cover finite circular space in a chamber. Multiple O-filters can be placed one behind another in a Hele-Shaw cell and can also be turned *on* or *off* independently in a cascade, without affecting the overall flow balance in the device.

V. CONCLUSION

Microfluidic surface shields can yield applications in fields where minimally disturbing surface-reconfigurable shielding is desired, in surface-based sensing technologies like surface-plasmon-resonance sensors [35]; whispering gallery-mode sensors [36]; quartz-crystal microbalance sensing [37]; and, in general, any assay where a target flows over a capture surface [5]. Given the strong mathematical analogy between mass and heat transport, they can also be used to alter temperature in a specific region of a device, while leaving the surroundings unaffected, or to dissipate heat locally, such as in chip-cooling applications [38]. At a much larger length scale, our results also apply to groundwater heat pumps, since flow and diffusion within them follow the same equations [25]. Finally, we hope that this work will inspire metamaterial-free methods to protect surfaces in various areas of physics, since the principles used here are applicable to any set of equations exhibiting natural conformal invariance, especially Laplace's equation, which encompasses every field of physics.

ACKNOWLEDGMENTS

This work is supported by a Fonds de Recherche du Québec – Nature et Technologie Team Grant (FRQNT, Grant No. 205993 2018). The authors also wish to acknowledge support from the National Science and Engineering Council of Canada (NSERC) for a Graham-Bell fellowship (E.B.) and a Discovery Grant (RGPIN, Grant No. 2020–06838). We thank David Juncker and Lucas Poncelet for useful dicussions and preliminary experimental support.

APPENDIX A: POTENTIAL MODEL FOR A RANKINE BODY IN A CHANNEL OF FINITE WIDTH

In the main text of the article, we assume that the source-sink doublet is placed in a chamber much larger than the interaperture distance, d, such that the walls of the chamber have little-to-no influence on the flow profile. We can, however, easily develop a complex potential model that takes into account the dimension of the chamber, for situations where it is comparable to the interaperture distance. This flow is still modeled using a complex potential and, as such, the walls are assumed to have slip flow. This is obviously different from the real-life situation, in which lateral walls undergo a no-slip boundary condition, but it

can be shown [39,40] that the effect of that no-slip condition is only on a small region of the order of the channel height near the wall, and the rest of the channel flow can be modeled as a potential flow without significant error. This approximation is justified in most Hele-Shaw cell applications, where the channel height is typically much smaller than both the interaperture distance and the chamber width.

The complex potential for the finite dipole in a finite chamber can be obtained in two ways. The first is to exploit the fact that slipping walls effectively act as symmetry boundary conditions. We can thus obtain a potential by the method of images by using an infinite sum of doublets. However, such a strategy yields expressions that are unwieldy and hard to manipulate. A more elegant method is to use a two-vertex Schwarz-Christoffel transformation.

Our starting domain is a semi-infinite plane with three point sources: one for the injection aperture, one for the aspiration aperture, and one that will be mapped to infinity and represents the incident flow. Calling our starting domain w, we have

$$\Phi_w = \frac{H}{2\pi}\beta \ln(w) + \ln\left[w - exp\left(-\frac{2\pi}{H}\right)\right] - \ln\left[w - exp\left(\frac{2\pi}{H}\right)\right]. \tag{A1}$$

We transform this potential using the two-vertex Schwarz-Christoffel map

$$w = exp\left(\frac{2\pi}{H}z\right), \tag{A2}$$

which maps the flow in the semi-infinite plane to the interior of a strip of width H, with apertures at $z = -1$ and $z = 1$, and a plane incident flow of velocity, β. The potential for the doublet source in the channel is thus given by

$$\Phi_z = \beta z + \ln\left[exp\left(\frac{2\pi}{H}z\right) - exp\left(-\frac{2\pi}{H}\right)\right] - \ln\left[exp\left(\frac{2\pi}{H}z\right) - exp\left(\frac{2\pi}{H}\right)\right]. \tag{A3}$$

A schematic representation of both domains is given in Fig. 5. A similar analysis to the one presented here can be used to obtain diffusion in this geometry. In cases where the chamber height is comparable to d but still larger than it, the same solution in the streamline domain can be used directly. However, for very small chamber heights, a different solution should be used, as the solution presented in the main text will breakdown due to contact between the interdiffusion zone and the walls of the chamber.

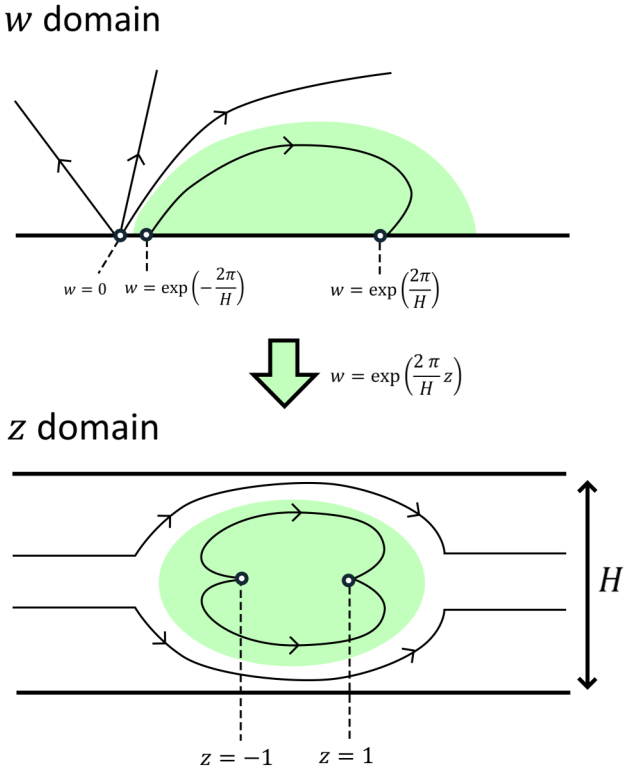

FIG. 5. Schematic representation of flow in the w and z domains.

APPENDIX B: MODELING PRESSURE RISE

In virtue of d'Alembert's paradox, a bidimensional obstacle moving at constant velocity in an inviscid and incompressible flow generates no pressure or velocity disturbance at a distance. However, the channel width is finite in our experiments and real fluids (having a nonzero viscosity) flow through it. Thus, even though the impediment undergoes a slip-boundary condition, just like a Rankine body, the incident fluid is pushed towards the lateral walls, which are no-slip boundaries, yielding an extra hydraulic resistance and, ultimately, a pressure rise. In this section, we present a model that links this pressure rise with the blockage ratio, which is defined as the ratio between the obstacle diameter and the chamber width.

Let us consider a viscid fluid obeying Stokes' equation and flowing in a Hele-Shaw cell. We suppose that, for obstacles much smaller than the channel width, the fluid velocity remains mainly horizontal when flowing around and past the impediment. In that case, the configuration is analogous to a fluid flowing in successive infinitesimally long rectangular channels, the widths of which are shortened due to the impediment's presence.

Assuming a slipping circular impediment of radius R placed in the middle of the chamber, the hydraulic resistance associated with the obstructed part of the channel can

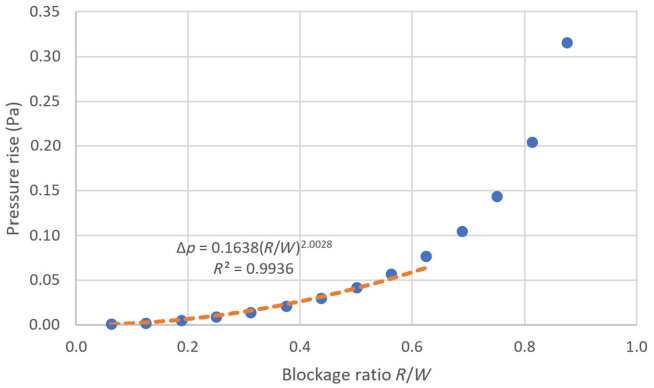

FIG. 6. Simulated pressure rises in the channel as a function of blockage ratio (dots). For small- and medium-blockage ratios, these data fit with a second-order model (dashed line).

be expressed as

$$R_H = \frac{12\mu}{G^3} R \int_0^{\pi} \frac{\sin(t)}{W - 0.63G - 2R\sin(t)} dt. \tag{B1}$$

After integration, given that $R \ll W - 0.63G$ (small obstacle) and considering that the pressure rise, Δp , obeys $\Delta p = R_H Q$, we get

$$\Delta p = \frac{12\mu\pi}{G^3}\left(\frac{R}{W - 0.63G}\right)^2 Q + o\left[\left(\frac{R}{W - 0.63G}\right)^2\right]. \tag{B2}$$

We see that there is neither zeroth-order nor first-order pressure disturbances generated by the obstacle. This quadratic law is confirmed by COMSOL simulations, even for moderate blockage ratios [Fig. 6]. For our microfluidic system, this means that the imperfection of pressure shielding can be made arbitrarily small either by making the Rankine body smaller or by fabricating wider devices.

APPENDIX C: PROBLEM IN STREAMLINE COORDINATES

The complex potential,

$$\Phi = \beta z + \ln(z + 1) - \ln(z - 1), \tag{C1}$$

allows us to transform our problem from the original experiment domain to the streamline coordinate domain, where the flow is a simple plane flow, and every feature of the original problem is translated to a horizontal segment. A map of the different segments of interest in the original domain and their image in streamline coordinates is given in Fig. 7, and the coordinates of each segment are given in Table I.

In Fig. 7 and Table I, z_{stag1} and z_{stag2} represent the two stagnation points of the flow, given by $z = \pm\sqrt{1 + 2/\beta}$,

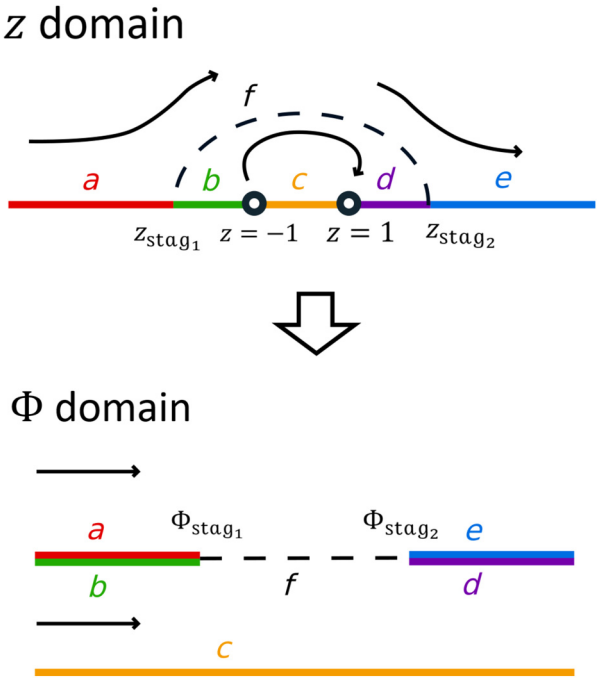

FIG. 7. Schematic of the flow in both the z domain and streamline domain.

and Φ_{stag1} and Φ_{stag2} represent the images of these points using the complex potential, Φ. There is no analytical expression for the separating segment f in the flow domain, but an implicit equation for it can be obtained using the expression for the complex potential.

The transformation to streamline coordinates also highlights the analogy between our O-filter and the well-known microfluidic H-filter. In both devices, fluids of two different concentrations are brought together, allowed to mix over a certain distance, then reseparated and collected. In the H-filter, the mixing region is the interdiffusion zone in the center of the channel, whereas in the O-filter, this zone is the contour of the Rankine body.

APPENDIX D: ELLIPTICAL APPROXIMATION OF FOOTPRINT

We consider the nondimensional potential introduced in the main text: $\Phi(z) = \beta z + \ln(z + 1) - \ln(z - 1)$. The contour of the Rankine body obeys $\psi(z) = 0$; however, without further hypotheses such an expression does not yield any usual geometrical objects. To get simpler models, we approximate the footprint as an ellipse and consider its horizontal "major axis" and vertical "minor axis."

The major axis is defined as the distance between the upstream and downstream stagnation points and is obtained by finding the zeros of the complex-velocity function. Thus, it can be found by solving $\Phi'(z) = 0$, which gives $z = \pm\sqrt{1 + 2/\beta}$. Therefore, the major axis is simply equal to $2\sqrt{1 + 2/\beta}$.

TABLE I. Features of the Rankine-body domain and its coordinates in the streamline domain.

Segment	Z-domain coordinates	Streamline-domain coordinates	Boundary condition
a	$x \in \left]-\infty, z_{\text{stag1}}\right[$ $y = 0$	$\phi \in \left]-\infty, \phi_{\text{stag1}}\right[$ $\psi = 0^+$	Symmetry
b	$x \in \left]z_{\text{stag1}}, -1\right[$ $y = 0$	$\phi \in \left]-\infty, \phi_{\text{stag1}}\right[$ $\psi = 0^-$	Symmetry
c	$x \in \left]-1, 1\right[$ $y = 0$	$\phi \in \left]-\infty, \infty\right[$ $\psi = 0^-$	Symmetry
d	$x \in \left]1, z_{\text{stag2}}\right[$ $y = 0$	$\phi \in \left]\phi_{\text{stag2}}, \infty\right[$ $\psi = 0^-$	Symmetry
e	$x \in \left]z_{\text{stag2}}, \infty\right[$ $y = 0$	$\phi \in \left]\phi_{\text{stag2}}, \infty\right[$ $\psi = 0^+$	Symmetry
f	No simple analytical form	$\phi \in \left]-\infty, \infty\right[$ $\psi = -\frac{\pi}{\beta}$	Continuity

For its part, the minor axis indicates the maximal width of the shielded region perpendicularly to the incident-flow direction and can be found by studying the contour lines of the stream function. It verifies $\psi(iy) = 0$, which can be written as $y + \arg(iy + 1) - \arg(iy - 1) = 0$. Contrary to the major axis, this is an implicit function that we need to solve numerically.

Experimentally speaking, the major and minor axes can be extracted by finding points belonging to the contour, $c = 1/2$ (which corresponds to the Rankine-body edge for high Pe), and by fitting an ellipse on those points thanks to a least-squares method. The ellipse's major and minor axes obtained with this approach are very good estimates of the Rankine body's horizontal and vertical extensions. A comparison of the elliptical approximation and experimental results are included in Fig. 8.

APPENDIX E: SHIELDING OF FINITE-SIZED OBJECTS

In the main text of the article, we present experimental and theoretical results for shielding setups in which the incident flow is at a fixed concentration (for example, $C = 0$), and the injected flow is at another concentration, $C = 1$. This is slightly different from what a practical shielding application would look like.

In a more "concrete" shielding application, we are trying to protect a finite object, for example, a diffusive (or absorbing) patch located at the bottom of the channel, such as those described in Ref. [3]. In a "worst-case" scenario, this patch can be modeled as having a fixed concentration, $C = 1$, which never gets depleted. In that case, in the absence of a recirculation zone, it generates a wake in the channel given by the convolution of the known Green's function [41] and a weighted kernel on its shape:

$$G(x, y) = \frac{e^{\text{Pe}\, x}}{2\pi} K_0\left(\text{Pe}\sqrt{x^2 + y^2}\right). \tag{E1}$$

The exact determination of the kernel is a nontrivial problem (see, for example, Refs. [42] or [30]) but the Green's function by itself can give a good estimate of the shape of the wake in the far field. We mention here that such a concentrated "obstacle" is located on the bottom surface of the channel and, as such, does not disturb the flow. It does, however, leave a significant wake behind it. By placing a Rankine body over such a concentrated patch, an important portion of the wake can be reabsorbed and prevented from disturbing the downstream concentration. Moreover,

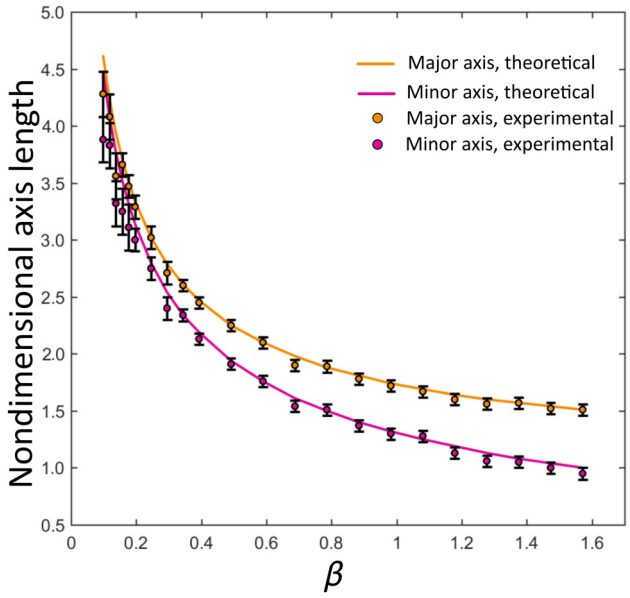

FIG. 8. Minor and major axes of the Rankine body and comparison with an approximate theoretical outline. Approximate outline is given by approximating the separating line as an ellipse. Horizontal intercepts are matched to the stagnation points, and vertical intercepts are obtained by finding the intercept of the separating streamline and the vertical axis.

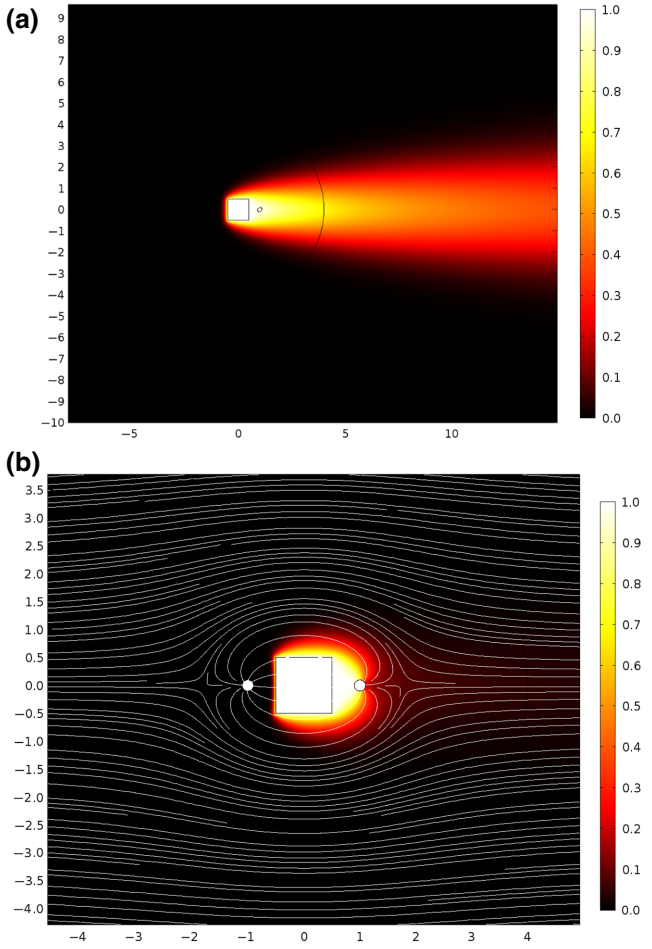

FIG. 9. Reabsorption of the wake by a finite reactive patch. (a) Wake in a plane flow left by a square patch of fixed concentration at Pe = 10. (b) Same reactive patch with the shielding device turned *on*. Wake is entirely reabsorbed by the Rankine body. Streamlines overlaid on the plot for clarity. Results are obtained using finite-element simulations of the 2D convection-diffusion equation.

if the device is dimensioned properly, the entirety of the wake can be reabsorbed.

In such a situation, we can see that the fraction of reagent that fails to be reabsorbed by the aspiration aperture is much smaller than in the worst-case scenario, where the entire injected fluid is at a concentration of $C = 1$. We can see through simple scaling arguments that, if the distance between the edge of the concentrated patch and the Rankine body's separating line is larger than two or three characteristic diffusion distances, the entirety of the diffusive species will be reabsorbed by the aspiration aperture.

This reabsorption of the wake generated by a finite patch is illustrated in Fig. 9. The results are obtained using finite-element simulations of the 2D convection-diffusion equation. An exact theoretical form for these wakes will have to be obtained by convolution of the Green's function

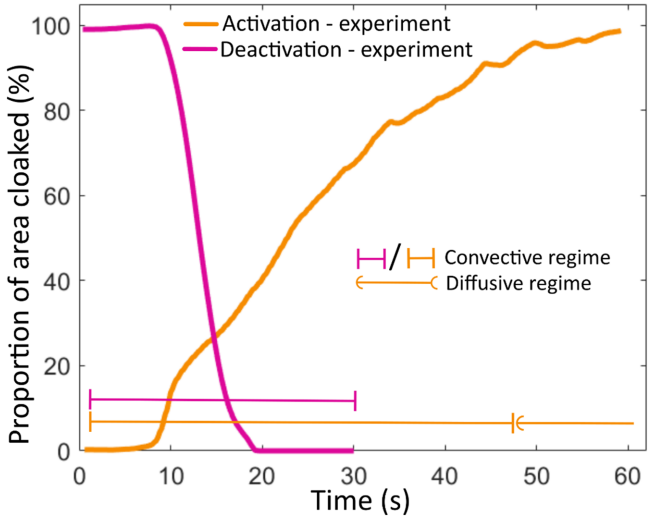

FIG. 10. Activation and deactivation kinetics of the device. As aspiration is turned *off*, the shielded area drops significantly, following convection of the concentrated area away from the Rankine body. As aspiration is turned back *on*, the shielded area is established following a convective regime first, then the Rankine body diffuses following the characteristic diffusion timescale.

and an integral kernel, which will have to be determined as part of the problem.

APPENDIX F: ACTIVATION AND DEACTIVATION KINETICS

As explained in the main text, we notice that activation kinetics (that is, the time it takes for the shielded region to be established) is controlled by the convective timescale, while the deactivation is split in two regimes: the first one is dominated by convective effects and the second one is controlled by the diffusive timescales. To illustrate these effects, we show in Fig. 10 the proportion of the surface under the footprint as a function of time in both activation and deactivation experiments.

[1] K. F. Jensen, Microreaction engineering—is small better? Chem. Eng. Sci. **56**, 293 (2001).
[2] R. H. Salman, K. M. Abed, and H. A. Hassan, Energy generation by membraneless microfluidic fuel cell using acidic wastewater as a fuel, Int. J. Ambient Energy **42**, 847 (2021).
[3] T. M. Squires, R. J. Messinger, and S. R. Manalis, Making it stick: Convection, reaction and diffusion in surface-based biosensors, Nat. Biotechnol. **26**, 417 (2008).
[4] R. Van Erp, R. Soleimanzadeh, L. Nela, G. Kampitsis, and E. Matioli, Co-designing electronics with microfluidics for more sustainable cooling, Nature **585**, 211 (2020).
[5] T. Gervais and K. F. Jensen, Mass transport and surface reactions in microfluidic systems, Chem. Eng. Sci. **61**, 1102 (2006).

[6] U. Leonhardt, Optical conformal mapping, Science **312**, 1777 (2006).

[7] J. B. Pendry, D. Schurig, and D. R. Smith, Controlling electromagnetic fields, Science **312**, 1780 (2006).

[8] S. A. Cummer and D. Schurig, One path to acoustic cloaking, New J. Phys. **9**, 45 (2007).

[9] H. Chen and C. Chan, Acoustic cloaking in three dimensions using acoustic metamaterials, Appl. Phys. Lett. **91**, 183518 (2007).

[10] M. Farhat, S. Guenneau, and S. Enoch, Ultra Broadband Elastic Cloaking in Thin Plates, Phys. Rev. Lett. **103**, 024301 (2009).

[11] N. Stenger, M. Wilhelm, and M. Wegener, Experiments on Elastic Cloaking in Thin Plates, Phys. Rev. Lett. **108**, 014301 (2012).

[12] S. Brûlé, E. Javelaud, S. Enoch, and S. Guenneau, Experiments on Seismic Metamaterials: Molding Surface Waves, Phys. Rev. Lett. **112**, 133901 (2014).

[13] M. Farhat, S. Enoch, S. Guenneau, and A. Movchan, Broadband Cylindrical Acoustic Cloak for Linear Surface Waves in a Fluid, Phys. Rev. Lett. **101**, 134501 (2008).

[14] S. Zhang, D. A. Genov, C. Sun, and X. Zhang, Cloaking of Matter Waves, Phys. Rev. Lett. **100**, 123002 (2008).

[15] R. Schittny, M. Kadic, S. Guenneau, and M. Wegener, Experiments on Transformation Thermodynamics: Molding the Flow of Heat, Phys. Rev. Lett. **110**, 195901 (2013).

[16] S. Guenneau, C. Amra, and D. Veynante, Transformation thermodynamics: Cloaking and concentrating heat flux, Optics Express **20**, 8207 (2012).

[17] F. Avanzini, G. Falasco, and M. Esposito, Chemical cloaking, Phys. Rev. E **101**, 060102(R) (2020).

[18] Y. A. Urzhumov and D. R. Smith, Fluid Flow Control With Transformation Media, Phys. Rev. Lett. **107**, 074501 (2011).

[19] H. S. Hele-Shaw, Flow of water, Nature **58**, 1509 (1898).

[20] P.-A. Goyette, E. Boulais, F. Normandeau, G. Laberge, D. Juncker, and T. Gervais, Microfluidic multipoles theory and applications, Nat. Commun. **10**, 1 (2019).

[21] E. Boulais and T. Gervais, Two-dimensional convection–diffusion in multipolar flows with applications in microfluidics and groundwater flow, Phys. Fluids **32**, 122001 (2020).

[22] B. H. Weigl and P. Yager, Microfluidic diffusion-based separation and detection, Science **283**, 5400 (1999).

[23] I. Watts, W. J. M. Rankine, F. K. Barnes, and J. R. Napier, *Shipbuilding, Theoretical and Practical* (William Mackenzie, London, 1866).

[24] J. Luo and P. K. Kitanidis, Fluid residence times within a recirculation zone created by an extraction–injection well pair, J Hydrol. **295**, 149 (2004).

[25] R. Weijermars and A. Van Harmelen, Breakdown of doublet recirculation and direct line drives by far-field flow in reservoirs: Implications for geothermal and hydrocarbon well placement, Geophys. J. Int. **206**, 19 (2016).

[26] F. Paratore, E. Boyko, G. V. Kaigala, and M. Bercovici, Electroosmotic Flow Dipole: Experimental Observation and Flow Field Patterning, Phys. Rev. Lett. **122**, 224502 (2019).

[27] P. Zhao and S. Rodriguez, Journal of Fluorescence **7**, 121 (1997).

[28] G. Grimberg, W. Pauls, and U. Frisch, Genesis of d'alembert's paradox and analytical elaboration of the drag problem, Phys. D **237**, 1878 (2008).

[29] M. Z. Bazant, Conformal mapping of some non-harmonic functions in transport theory, Proc. R. Soc. London, Ser. A **460**, 1433 (2004).

[30] J. Choi, D. Margetis, T. M. Squires, and M. Z. Bazant, Steady advection-diffusion around finite absorbers in two-dimensional potential flows, J. Fluid Mech. **536**, 155 (2005).

[31] M. Cummings, Y. E. Hohlov, S. D. Howison, and K. Kornev, Two-dimensional solidification and melting in potential flows, J. Fluid Mech. **378**, 1 (1999).

[32] M. Safavieh, M. A. Qasaimeh, A. Vakil, D. Juncker, and T. Gervais, Two-aperture microfluidic probes as flow dipoles: Theory and applications, Sci. Rep. **5**, 1 (2015).

[33] J. P. Brody, P. Yager, R. E. Goldstein, and R. H. Austin, Biotechnology at low reynolds numbers, Biophys. J. **71**, 3430 (1996).

[34] L. G. Leal, *Advanced Transport Phenomena: Fluid Mechanics and Convective Transport Processes* (Cambridge University Press, Cambridge, 2007), Vol. 7, pp. 666–668.

[35] J. Homola, S. S. Yee, and G. Gauglitz, Surface plasmon resonance sensors, Sens. Actuators, B **54**, 3 (1999).

[36] M. R. Foreman, J. D. Swaim, and F. Vollmer, Whispering gallery mode sensors, Adv. Opt. Photonics **7**, 168 (2015).

[37] J. Auge, P. Hauptmann, F. Eichelbaum, and S. Rösler, Quartz crystal microbalance sensor in liquids, Sens. Actuators, B **19**, 518 (1994).

[38] E. M. Dede, F. Zhou, P. Schmalenberg, and T. Nomura, Thermal metamaterials for heat flow control in electronics, J. Electron. Packag. **140**, 010904 (2018).

[39] H. Bruus, *Theoretical Microfluidics* (Oxford University Press, Oxford, 2007), Vol. 18, pp. 50.

[40] O. Gökçe, S. Castonguay, Y. Temiz, T. Gervais, and E. Delamarche, Self-coalescing flows in microfluidics for pulse-shaped delivery of reagents, Nature **574**, 228 (2019).

[41] A. D. Polyanin, *Handbook of Linear Partial Differential Equations for Engineers and Scientists* (Chapman and Hall/CRC, London, 2001).

[42] C. E. Pearson, On the finite strip problem, Q. Appl. Math. **15**, 203 (1957).